A&A 441, 905–914 (2005)
DOI: 10.1051/0004-6361:20042544

Astronomy & Astrophysics

GaBoDS: the Garching-Bonn Deep Survey

III. Lyman-break galaxies in the Chandra Deep Field South⋆,⋆⋆

H. Hildebrandt[1], D. J. Bomans[2], T. Erben[1], P. Schneider[1], M. Schirmer[3], O. Czoske[1], J. P. Dietrich[1], T. Schrabback[1], P. Simon[1], R. J. Dettmar[2], L. Haberzettl[2], M. Hetterscheidt[1], and O. Cordes[1]

[1] Institut für Astrophysik und extraterrestrische Forschung, Universität Bonn, Auf dem Hügel 71, 53121 Bonn, Germany
e-mail: hendrik@astro.uni-bonn.de
[2] Astronomisches Institut der Ruhr-Universität-Bochum, Universitätsstr. 150, 44780 Bochum, Germany
[3] Isaac Newton Group of Telescopes, Apartado de correos 321, 38700 Santa Cruz de La Palma, Tenerife, Spain

Received 15 December 2004 / Accepted 23 June 2005

ABSTRACT

We present first results of our search for high-redshift galaxies in deep CCD mosaic images. As a pilot study for a larger survey, very deep images of the Chandra Deep Field South (CDFS), taken with WFI@MPG/ESO2.2m, are used to select large samples of 1070 U-band and 565 B-band dropouts with the Lyman-break method. The data of these Lyman-break galaxies are made public as an electronic table. These objects are good candidates for galaxies at $z \sim 3$ and $z \sim 4$ which is supported by their photometric redshifts. The distributions of apparent magnitudes and the clustering properties of the two populations are analysed, and they show good agreement to earlier studies. We see no evolution in the comoving clustering scale length from $z \sim 3$ to $z \sim 4$. The techniques presented here will be applied to a much larger sample of U-dropouts from the whole survey in near future.

Key words. galaxies: photometry – galaxies: high-redshift – surveys

1. Introduction

In order to constrain models of structure formation and to investigate the star formation history of the universe, large samples of galaxies at high redshift are needed. The clustering properties on large scales at these high redshifts can only be studied with contiguous fields of considerable size. Furthermore, to overcome cosmic variance, different lines of sight should be probed. The Lyman-break technique is an efficient method to select galaxies at high redshift from multi-colour optical data.

The largest survey of Lyman-break galaxies (LBGs) at $z \sim 3$ to date (Steidel et al. 2003) covers 0.38 square degrees in 17 widely separated fields yielding more than 2000 LBG candidates of which 940 have been confirmed spectroscopically. On a sub-area, this group has published 244 G-dropouts (48 spectroscopically confirmed), candidates for $z \sim 4$ galaxies (Steidel et al. 1999). Foucaud et al. (2003) published results from the Canada-France deep fields identifying ∼1300 U-dropouts on a shallower but larger field. Very recently, Ouchi et al. (2004a) obtained a sample of ∼2000 B-dropouts in deep Suprime-Cam imaging and observed 85 of them spectroscopically.

In this paper we investigate large samples of U- and B-dropouts in very deep wide-field images of the CDFS. This investigation on one field is a pilot study for a much larger survey, the ESO Deep-Public-Survey (DPS), of LBGs on mosaic CCD data. Special attention is paid to the careful selection of candidates and the comparison with other successful studies of LBGs. While still smaller than some other samples because of the limited area, our LBG population will grow significantly in the near future with the analysis of the whole survey. Here the methods that will be applied to the complete dataset are presented and evaluated.

In Sect. 2 the observations, the data reduction, and the catalogue extraction are described. Section 3 deals with the photometric selection of dropouts in our data. After that the properties of the two dropout samples are presented in Sect. 4. Photometric redshift estimates, the distributions of apparent magnitudes, and the clustering properties are shown there. Concluding remarks and an outlook are given in Sect. 5.

2. Observations and data reduction

2.1. Observations

The Chandra Deep Field South ($\alpha = 03^{\rm h}\,32^{\rm m}\,29^{\rm s}$, $\delta = -27^\circ\,48'\,47''$) was observed with the WFI@MPG/ESO2.2m

⋆ Based on observations made with ESO Telescopes at the La Silla Observatory.
⋆⋆ Tables A.1 and A.2 are only available in electronic form at the CDS via anonymous ftp to
cdsarc.u-strasbg.fr (130.79.128.5) or via
http://cdsweb.u-strasbg.fr/cgi-bin/qcat?J/A+A/441/905

Table 1. Properties of the CDFS WFI-data. The limiting magnitudes in Cols. 3 and 4 are calculated with Eq. (1).

Band	ESO-Id	Exposure time [s]	3σ limits in a $2''$ diam. aperture (Vega mags)	1σ limits in $2 \times FWHM$ diam. (Vega mags)	AB correction	$FWHM$ [$''$]	Source
U	U/50	43 600	25.6	26.8	0.9	1.07	EIS
B	B/99	57 000	28.0	29.2	−0.1	0.99	Bonn/GaBoDS
V	V/89	56 000	27.5	28.7	0.0	0.93	Bonn/GaBoDS
R	Rc/162	57 100	27.6	28.7	0.2	0.81	Bonn/GaBoDS
I	Ic/lwp	26 900	25.1	26.3	0.5	0.95	EIS

for several programmes. Data were taken for the GOODS project (Giavalisco et al. 2004), the COMBO-17 survey (Wolf et al. 2004), and the ESO-Imaging-Survey (EIS) (Arnouts et al. 2001). All these data are available from the ESO archive. Erben et al. (ESO Press Photos 02a-d/03) have produced very deep images in *BVR* with a field-of-view of $34' \times 33'$ using the Bonn WFI reduction pipeline (Schirmer et al. 2003; Erben et al. 2005). Additionally, U- and I-band images were published by the EIS-team (Arnouts et al. 2001). Their properties are summarised in Table 1[1].

The *BVR* images were coadded with *drizzle* (Fruchter & Hook 2002). The astrometric calibration was done with respect to the USNO-A2.0 (Monet et al. 1998) and the photometric calibration is based on the COMBO-17 CDFS data (Wolf et al. 2004).

The properties of the U- and I-band images from EIS are described in detail in Arnouts et al. (2001). The astrometric solution for these images is recalculated on the basis of our R-band catalogue.

2.2. Image preparation and catalogue extraction

Since the EIS images come from a different reduction pipeline it is necessary to resample them again to exactly the same output grid with the same centre coordinates in order to use the dual image mode of *SExtractor* (Bertin & Arnouts 1996) described below. This is done by *SWarp* (Bertin 2003) which minimises the introduction of additional noise by applying a reverse mapping technique combined with an advanced kernel function (Lanczos-3).

The catalogues are created using *SExtractor* in dual-image mode. In this mode objects are detected and their shapes are measured on the R-band image. The flux in the other bands is measured on the corresponding images at the positions derived from the R-band. The R-band is chosen as the detection image since it is very deep, has very good seeing, and the targeted LBGs are comparatively bright in this band. An object is detected in the R-band if the flux in five adjacent pixels exceeds the standard deviation of the local sky background fluctuations by a factor of three. This conservative criterion is chosen because the handling of dropouts in blue bands requires clear detections in redder bands.

To account for the different seeing properties of the images, aperture magnitudes are used with the size of the aperture in one band scaled to the seeing of that image (diameter of the aperture = $2 \times FWHM$) when colours are measured. This approach is justified for the investigation of LBGs since these objects are usually not resolved in ground-based images. Thus, our approach delivers correct colours as long as the seeing is not too different in the images used (see Table 1). When magnitudes are cited in the following, the *SExtractor* parameter MAG_AUTO is used which corresponds to flexible elliptical apertures described in Kron (1980). The aperture magnitudes are used only for colour estimation.

When objects are detected in the R-band image and the flux is measured in the other bands, it is necessary to separate detected from non-detected objects in the bands different from the R-band. For that purpose limiting magnitudes for the apertures defined above are calculated:

$$mag_{\rm lim} = ZP - 2.5 \log\left(\sqrt{N_{\rm pix}} \cdot \sigma\right). \quad (1)$$

ZP is the photometric zeropoint of the image, $N_{\rm pix}$ is the number of pixels in the aperture, and σ gives the global rms pixel-to-pixel fluctuations of the sky background in the image considered. In Table 1 two different limiting magnitudes are given for every image, 3σ limits in a $2''$ diameter aperture and the 1σ limits in an aperture with $2 \times FWHM$ diameter. The latter are used to set a lower/upper limit to the colour index of objects that are not detected in one band.

Our final catalogue contains ∼57 000 R-band detected objects of which ∼10 000 have no significant flux in U, ∼300 are not detected in B, <100 are not detected in V (mostly R-band image defects), and ∼4500 are not detected in I (due to the shallower depth of this image). No star-galaxy separation is performed. LBGs are of such small apparent size that a considerable fraction of them would possibly be misclassified as stars and rejected if this was done.

3. Sample selection

Whenever selecting a sub-population from a large catalogue, attention must be paid to maximise completeness and efficiency. Often these goals are working in opposite directions and a good compromise must be chosen. While the real efficiency can usually be quantified with spectroscopic data at hand, the completeness is hard to quantify. Even defining completeness and efficiency can be somewhat ambiguous in this context as we show in the following. Here we are searching for high-redshift galaxies, which means that stars or low-redshift interlopers can contaminate the catalogues, thus reducing the efficiency. The case for intermediate redshift ($1 < z < 2$) galaxies is more difficult. In principle, we are highly interested in these objects since few are known up to now (see

[1] If not otherwise specified we use Vega magnitudes in this paper.

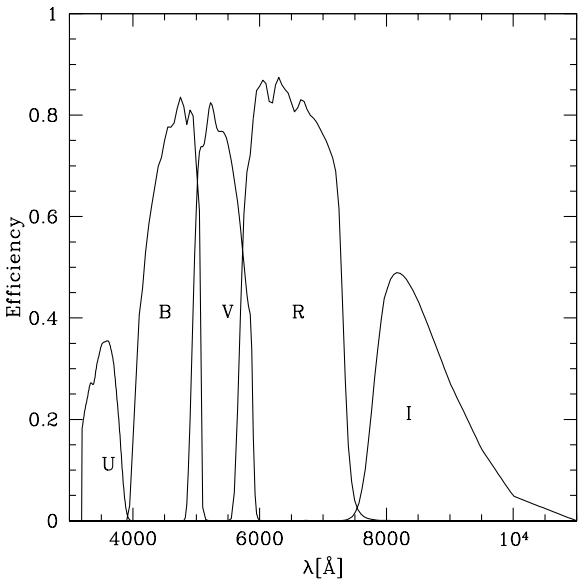

Fig. 1. Instrumental response of WFI in the different filters.

Steidel et al. 2004). But for the clustering analysis and obtaining luminosity functions in redshift slices, these objects are also contaminants and should be separated. To guarantee a reasonable efficiency, model galaxies' colours are investigated for high-redshift galaxies with a pronounced Lyman-break as well as for low-redshift ellipticals that are nearby in colour space. Furthermore, our selection follows other successful studies of LBGs cited above.

Completeness, however, is a different issue. If our goal was to select every galaxy at e.g. $z \sim 3$ in our data we would not be very complete with the method described below. In fact we are searching for LBGs which are easy to detect because of their pronounced Lyman-break. More dusty galaxies are much harder to separate from low-redshift objects, and if they are common at high redshift we will miss a lot of them with our selection criteria. Today it is known that LBGs are common at high redshift and not rare objects, representing a considerable fraction of the total galaxy population at these epochs (Giavalisco 2002).

3.1. Colours of high-redshift galaxies

The publicly available photometric redshift code *Hyperz* (Bolzonella et al. 2000) is used to estimate the colours of high-redshift galaxies. Template spectra from the library of Bruzual & Charlot (1993) are taken and convolved with the instrumental response of the WFI (see Fig. 1). The spectral energy distribution (SED) of a galaxy with constant star formation rate (spectral type: Im) is chosen which has a pronounced Lyman-break. Different amounts of reddening are taken into account by applying the dust extinction law of Calzetti et al. (2000). The opacity of the intergalactic medium is included by applying the estimates from Madau (1995).

Furthermore, the colours of elliptical galaxies at low redshift are calculated in an identical way in order to estimate their contamination of our samples of LBGs. In Fig. 2 the colour distributions of the model galaxies are shown.

3.2. Selection of candidates

We based our selection criteria for high-redshift objects on the predicted colours of model galaxies as outlined above. Given our filter set (see Fig. 1) and the data quality in the different bands, objects with $z \sim 3$ are selected most efficiently in a $U-V$, $V-R$ colour–colour diagramme. More distant galaxies at $z \sim 4$ are preferentially picked up in the $B-R$, $R-I$ space. In principle those populations can also be selected in $U-B$, $B-V$ and $B-V$, $V-R$ space respectively. However, due to the significant wavelength overlaps between the B, V and R filters, and due to the small gap between U and B, an efficient discrimination between galaxies with and without a pronounced Lyman-break is not possible in such diagrammes. This can be seen in Fig. 3 where the redshift tracks run more diagonal than in Fig. 2 due to the fact that an object that "drops out" from the U-band completely becomes already significantly fainter in the B-band. For the same reason a search for V-dropouts in our data is difficult, although our very deep wide-field V-band is predestined for such a project. Deep infrared data from the GOODS project with ISAAC@VLT (Giavalisco et al. 2004) are available for the innermost part of our field and will help in searching for V-dropouts (see Sect. 5).

The selection must always be a compromise between completeness and efficiency. Galaxies that are too red in $V-R$ cannot be included in the $z \sim 3$ selection box, for example, if one wants to avoid contamination by low-redshift elliptical galaxies. The same is true for the $z \sim 4$ sample. Photometric errors will scatter the data-points of faint galaxies around in the two-colour-diagrammes so that it is not possible to predict a precise redshift distribution of the samples. Furthermore, the redshift distribution will change with intrinsic spectral shape because of complex selection effects.

Based on these considerations the following selection criteria are chosen (see Fig. 2). For the U-dropout selection,

$$\begin{aligned} &1 \leq (U-V), \\ &-0.5 \leq (V-R) \leq 1.5, \\ &3 \cdot (V-R) \leq (U-V) - 0.5, \end{aligned} \tag{2}$$

and for the B-dropout selection,

$$\begin{aligned} &2 \leq (B-R), \\ &(R-I) \leq 1.5, \\ &2.5 \cdot (R-I) \leq (B-R) - 1.25. \end{aligned} \tag{3}$$

Applied to our catalogues, we get 1167 $z \sim 3$ U-dropout candidates and 613 $z \sim 4$ B-dropout candidates (see Fig. 5). All U-dropout candidates are detected in the B-, V-, and R-band images, so that their colour selection is not influenced by the depth of these images. 101 of them are not detected in I being fainter than $I = 26.3$, the detection limit in that band. The colour selection of the intrinsically fainter B-dropouts is also not seriously influenced by that effect, although 172 of them are not detected in I (this is the reason for the spike running from

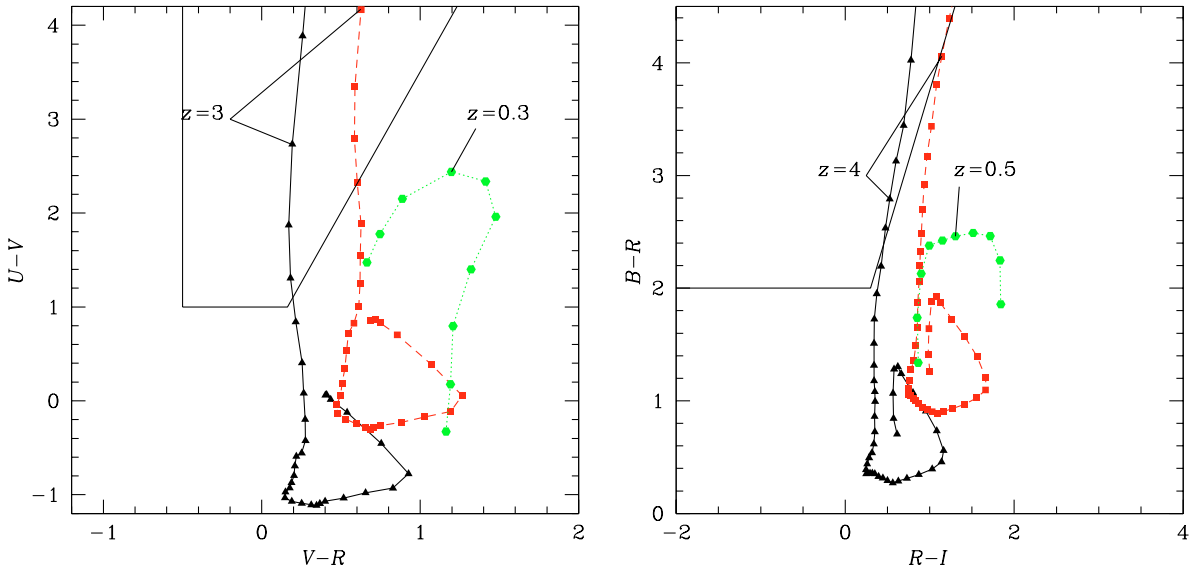

Fig. 2. Colours of model galaxies in the $U-V$ vs. $V-R$ two-colour diagramme used for U-dropout selection (*left*) and in the $B-R$ vs. $R-I$ two-colour diagramme for B-dropout selection (*right*). The solid lines represent galaxies (spectral type Im) with no dust reddening, the dashed lines represent galaxies (spectral type Im) with an extinction in the visual of $A_V = 1.5$ mag, and the dotted lines represent elliptical galaxies (spectral type E) at low redshift. The points correspond to intervals of $\Delta z = 0.1$. The boxes define our selection boundaries for high-z galaxy candidates.

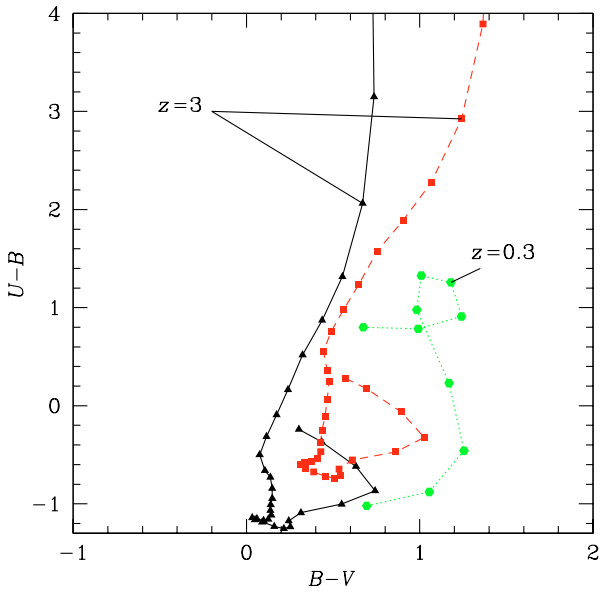

Fig. 3. Colours of model galaxies. The solid line represents galaxies (spectral type Im) with no dust reddening, the dashed line represents galaxies (spectral type Im) with an extinction in the visual of $A_V = 1.5$ mag, and the dotted lines represent elliptical galaxies (spectral type E) at low redshift. The points correspond to intervals of $\Delta z = 0.1$. Here the effect of overlapping filters can be seen, resulting in slightly diagonal tracks which make it difficult to choose a selection box.

the lower right to the upper left in the selection box of Fig. 5). Their $(R-I)$ colour is an upper limit. There are, however, some objects that lie to the right of our selection box, which could have bluer $(R-I)$ colours. So, efficiency is not affected while completeness suffers from the lower depth of the I-band image.

Thumbnail pictures in the five WFI bands are created for all selected objects. Some examples are shown in Figs. 6 and 7. Every candidate is checked by eye and some spurious detections like bad pixels, cosmic rays, reflections, or other image defects are rejected. After that our catalogues still contain 1070 U-dropouts and 565 B-dropouts. Our dropout catalogues are freely available to the scientific community via CDS (Tables A.1 and A.2). The spatial distribution of the two samples is shown in Fig. 4.

3.3. Observations with other telescopes

The whole WFI field is covered with data from the Advanced Camera for Surveys (ACS) on board Hubble Space Telescope (HST). The inner part of our $34' \times 33'$ field was observed for the GOODS programme (Giavalisco et al. 2004) in the four bands *BVIZ* (*F435W*, *F606W*, *F775W* and *F850LP*) and the outer regions were observed for the GEMS project (Rix et al. 2004) in V and Z (*F606W* and *F850LP*). From these data, thumbnail pictures for nearly every dropout candidate are created and examples are also shown in Figs. 6 and 7.

Since the GOODS data cover the *BVIZ* filters, they are suited to check our B-dropout selection criteria. The ACS thumbnails of all the B-dropouts inside the GOODS area are checked by eye for contamination by stars (point-like objects) or objects that are clearly visible in the ACS B-band image. Seven out of 66 objects are classified as possible contaminants. Thus, we roughly estimate the efficiency of our B-dropout selection to ∼90%.

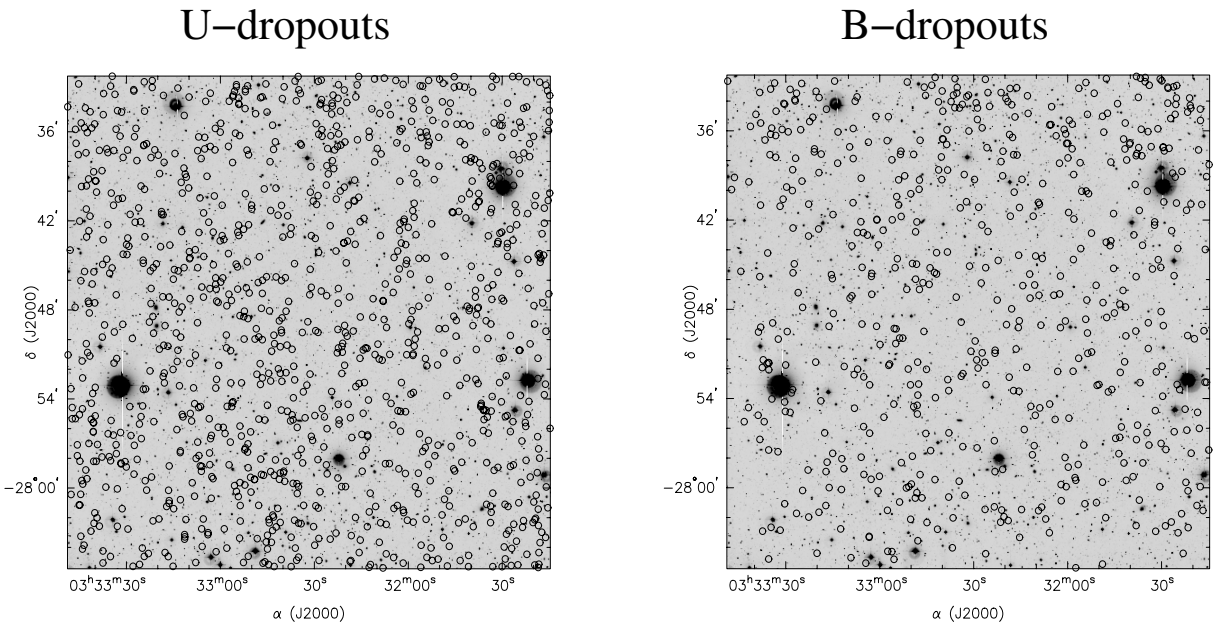

Fig. 4. Spatial distribution of our U-dropouts (*left*) and our B-dropouts (*right*).

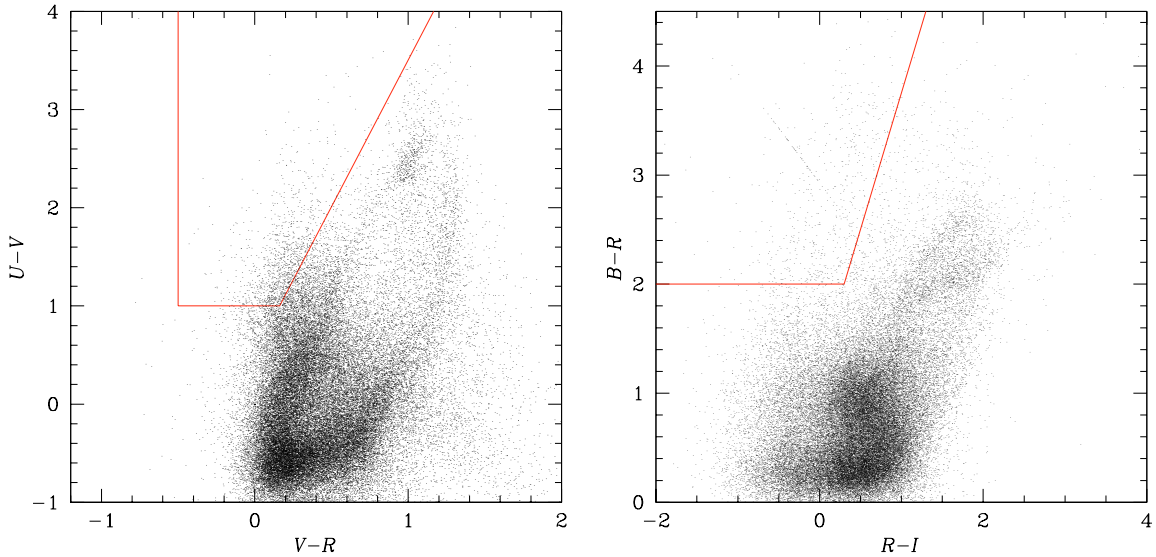

Fig. 5. $(U-V)$ vs. $(V-R)$ (*left*) and $B-R$ vs. $R-I$ (*right*) colours of galaxies in the CDFS WFI catalogue. The boxes represent the selection criteria given in equation 2 (*left*) and 3 (*right*). The spike running from the lower right to the upper left inside the B-dropout selection box (*right*) is an artifact due to the inferior depth of the I-band image (see text). It does not affect the efficiency of the dropout selection.

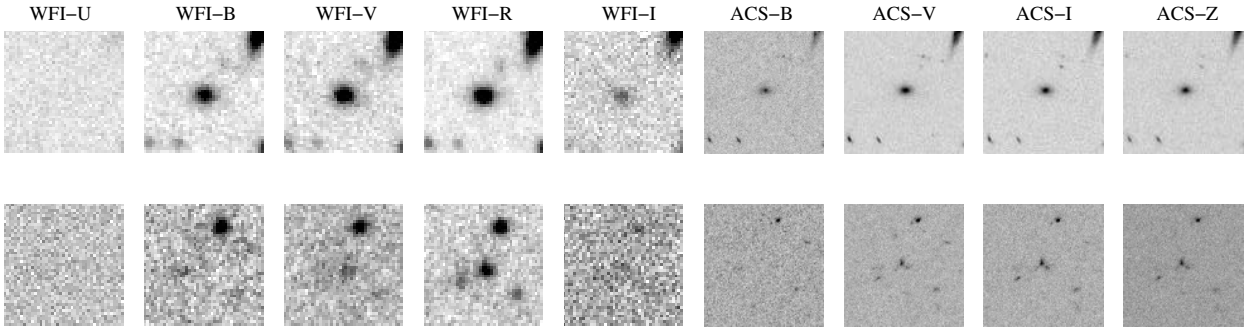

Fig. 6. Examples of a U-dropout (*upper row*) and a B-dropout (*lower row*) in the GOODS area. Thumbnail pictures in the WFI-*UBVRI* and ACS-*BVIZ* filters (*from left to right*) of size $10'' \times 10''$.

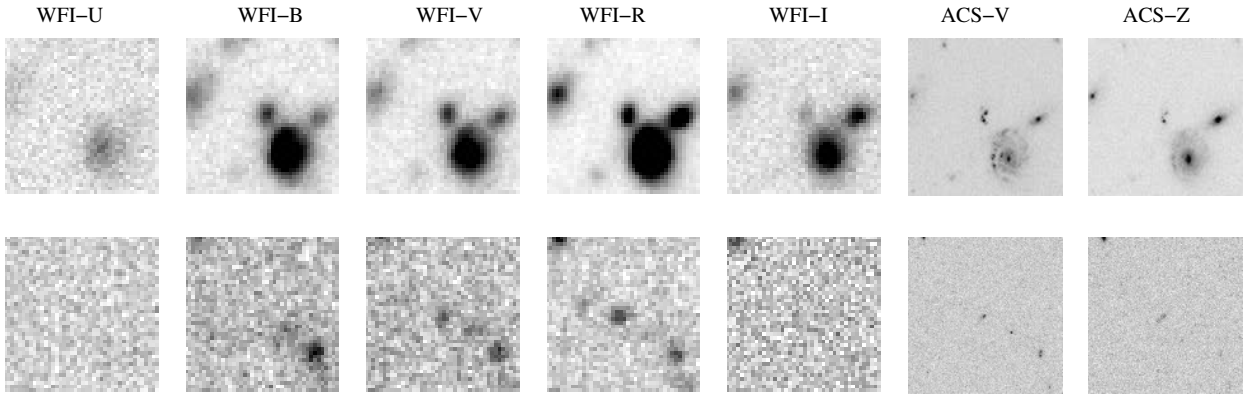

Fig. 7. Examples of a U-dropout (*upper row*) and a B-dropout (*lower row*) in the GEMS area. Thumbnail pictures in the WFI-$UBVRI$ and ACS-VZ filters (*from left to right*) of size $10'' \times 10''$. In the ACS images the irregular nature of this U-dropout is clearly revealed, while the B-dropout is barely visible in the WFI-I-band because of the limited depth of this image.

Six of our U-dropouts have been observed spectroscopically in the VVDS (Le Fèvre et al. 2004) and one of them also for the GOODS programme (Vanzella et al. 2005). Three of them are at $z > 3$, while the other three are low-redshift interlopers. This is not surprising since all of these objects are quite bright ($R \sim 23$) and contamination plays an important role in these magnitude ranges (see Steidel et al. 2003). The redshift of one of those interlopers is not yet determined unambiguously, estimates range from $z = 0.22$ (GOODS) to $z = 0.64$ (VVDS). None of our B-dropouts have been observed spectroscopically so far.

4. Properties of the samples

In this section we test our selection criteria in detail by analysing and comparing our LBG samples against those of other studies.

4.1. Photometric redshift distributions

Photometric redshifts for all candidates are estimated from their *UBVRI* photometry with the programme *Hyperz* (Bolzonella et al. 2000). Again the template SEDs by Bruzual & Charlot (1993) are chosen. The programme calculates galaxy colours in the WFI filter set at different redshifts for every template incorporating different ages, different amounts of reddening (Calzetti et al. 2000), and absorption by the Lyman-α forest (calculated in dependence of redshift according to Madau 1995). Every object is assigned the redshift of the best-fit SED, the primary solution phot-z. Furthermore, a weighted mean redshift is computed in the 99% confidence interval around the primary solution. The distributions of these quantities for all of our dropouts are shown in Fig. 8. There are clear peaks at the targeted redshifts of $z \sim 3$ and $z \sim 4$. Furthermore, there is a secondary peak in the redshift distribution of the U-dropouts at lower redshift ($z \sim 1.7$) which is more pronounced in the distribution of the primary redshifts and "washed-out" in the distribution of the weighted mean redshifts.

The programme *Hyperz* can also put out the probability (associated with the χ^2 value) of an object to be located at the different redshift values. Investigating these redshift-probability distributions of every single U-dropout with assigned redshift phot-$z < 2$ it becomes clear that for most of them no unique solution is found. There are multiple solutions (often another peak at $z \sim 3$) or plateaus (see Fig. 9), which results in a washed-out distribution of the weighted mean redshifts. For comparison, the unambiguous redshift probability distribution of an object with assigned redshift phot-$z = 3.29$ is also shown in Fig. 9. Most of the objects with assigned redshift phot-$z \sim 3$ show similar distributions even though not as perfect as this example.

It is possible that a significant fraction of those objects with phot-$z < 2$ are indeed LBGs at redshifts of 3, but are not unambiguously identified as such by *Hyperz*. This assumption is strengthened by the fact that the redshift-probability distribution of many of those galaxies shows a secondary peak at $z \sim 3$ (see Fig. 9).

In case those objects are indeed at a lower redshift of $z \sim 2$, they would fall into the so-called "redshift desert", where a determination of photometric and spectroscopic redshifts is very difficult due to the absence of prominent spectral features such as strong breaks in the *UBVRI* range.

Steidel et al. (2004) have identified a large number of galaxies in this so-called "redshift desert" applying a technique very similar to the Lyman-break technique with a selection box just below the LBG selection box (Adelberger et al. 2004). Photometric errors and differences in their and our filter set could scatter some lower redshift objects into our selection box. Some of these objects will certainly be included in the spectroscopic follow-up survey described in Sect. 5.

4.2. Distribution of apparent magnitudes

In order to compare our number-counts to other studies, the total R-band Vega magnitudes of the U-dropouts are converted to Steidel's $\mathcal{R}_{AB}$-band using the transformation equation in Steidel & Hamilton (1993) and an AB correction of 0.2 mag. The total I-band Vega magnitudes of the B-dropouts are converted to the AB system using an AB correction of 0.5 mag. Both AB corrections are calculated with *Hyperz* (Bolzonella et al. 2000). In Fig. 10 our results are shown in comparison to

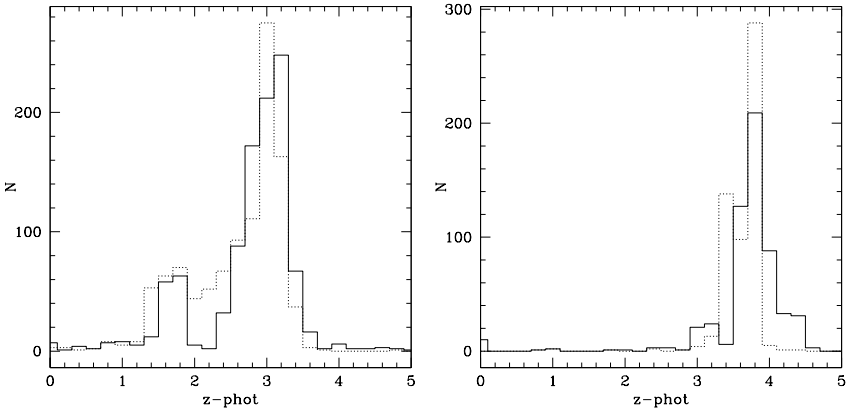

Fig. 8. Photometric redshift distributions of our U-dropouts (*left*) and our B-dropouts (*right*). The solid lines correspond to the distributions of the primary solutions and the dashed lines correspond to the distributions of the weighted mean redshifts (see text).

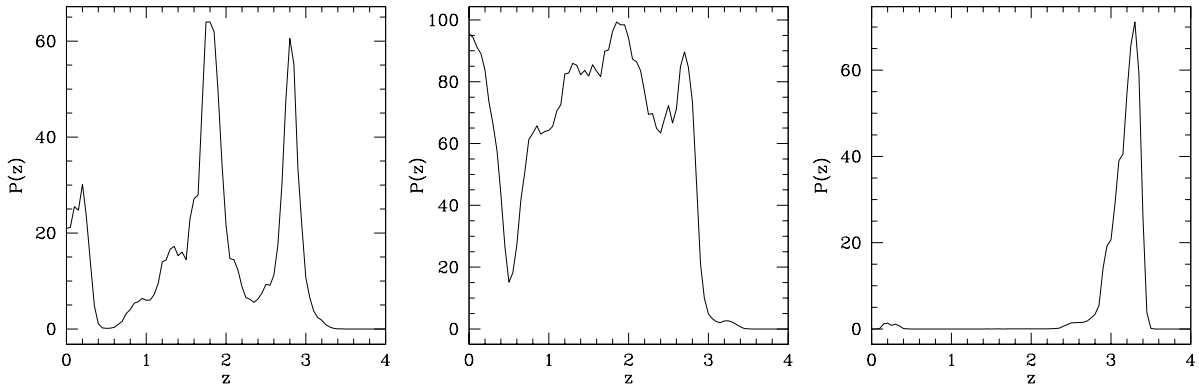

Fig. 9. Redshift vs. probability (associated with the χ^2 value) for three different U-dropouts. *Left*: an object with assigned redshift phot-z = 1.81. This example illustrates that the assignment of a single number for the photometric redshift can be misleading. The peak at $z = 2.8$ has nearly the same probability. *Middle*: an object with assigned redshift phot-z = 1.85. This example illustrates that sometimes the photometric redshift estimation totally fails but nevertheless a primary solution is put out. *Right*: an object with assigned redshift phot-z = 3.29. The ideal case of an object with a definite single redshift estimate.

Steidel et al. (1999). In general there is good agreement between the two studies.

The few deviations, however, can be explained. On the one hand, Steidel et al. (1999) correct their number-counts for contamination by low-z interlopers and stars using their large spectroscopic database which reduces the numbers at the brighter magnitudes. On the other hand, their images go slightly deeper (0.5−1 mag in the U-band depending on the field; see Steidel et al. 2003) which increases their number of LBGs at the faint end.

4.3. Angular correlation functions

For calculating the angular correlation function we apply the estimator by Landy & Szalay (1993),

$$\omega(\theta)\ \delta\theta = \frac{\mathrm{DD} - 2\mathrm{DR} + \mathrm{RR}}{\mathrm{RR}}. \quad (4)$$

DD, DR, and RR represent the number-counts of galaxy pairs with a separation between θ and $\theta + \delta\theta$ in catalogues extracted from the data (DD), from a random distribution of galaxies (RR) with the same survey geometry (including masked out regions), and between data and random catalogues (DR). The errors of the angular correlation function are estimated following the Poissonian variance approach of Landy & Szalay (1993), which is justified in the weak clustering regime,

$$\delta\omega(\theta) = \sqrt{\frac{1 + \omega(\theta)}{\mathrm{DD}}}. \quad (5)$$

A power law $\omega(\theta) = A_\omega\, \theta^{-\delta}$ with fixed slope $\delta = 0.8$ is fitted to the data for angular scales smaller than ∼2.′5. For larger scales the finite size of the fields begins to play a role which can be accounted for by an additional constant called "integral constraint". In Fig. 11, the angular correlation functions for the U- and B-dropouts are shown, the latter still suffering from small number statistics. The power law fits to our data yield amplitudes for a scale of 1″ of $A_\omega = 0.71 \pm 0.13$ for the U-dropouts and $A_\omega = 2.31 \pm 0.78$ for the B-dropouts, respectively.

Next, we discuss the influence of inhomogeneous depth in our data on the correlation analysis. All of our U-dropouts are brighter than $R = 26$ and $V = 25.8$. Given the depth of the V- and R-band image (see Table 1) small fluctuations in limiting magnitude over the field will have no impact on our selection. In the U-band image, however, there are some regions which are significantly shallower and could influence our selection. At the left edge there is a vertical stripe and in the middle there is a horizontal stripe where the 1σ limiting

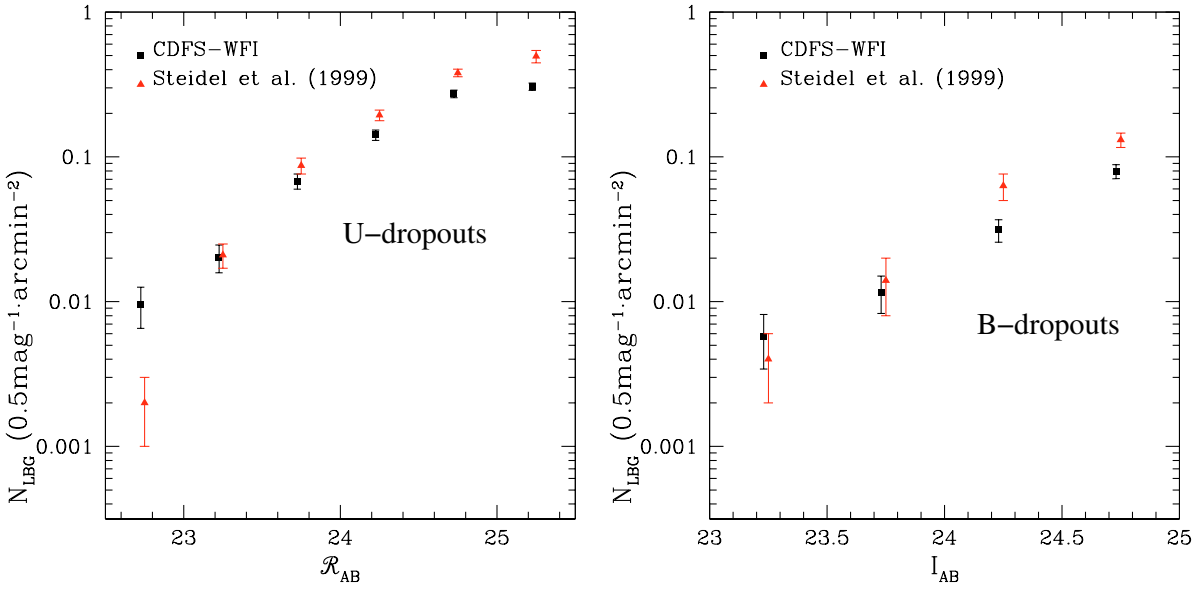

Fig. 10. The diagrammes show number-counts for U-dropouts (*left*) and B-dropouts (*right*) of our catalogue (squares) and that of Steidel et al. (1999) (triangles). The CDFS-WFI data points are slightly offset for clarity.

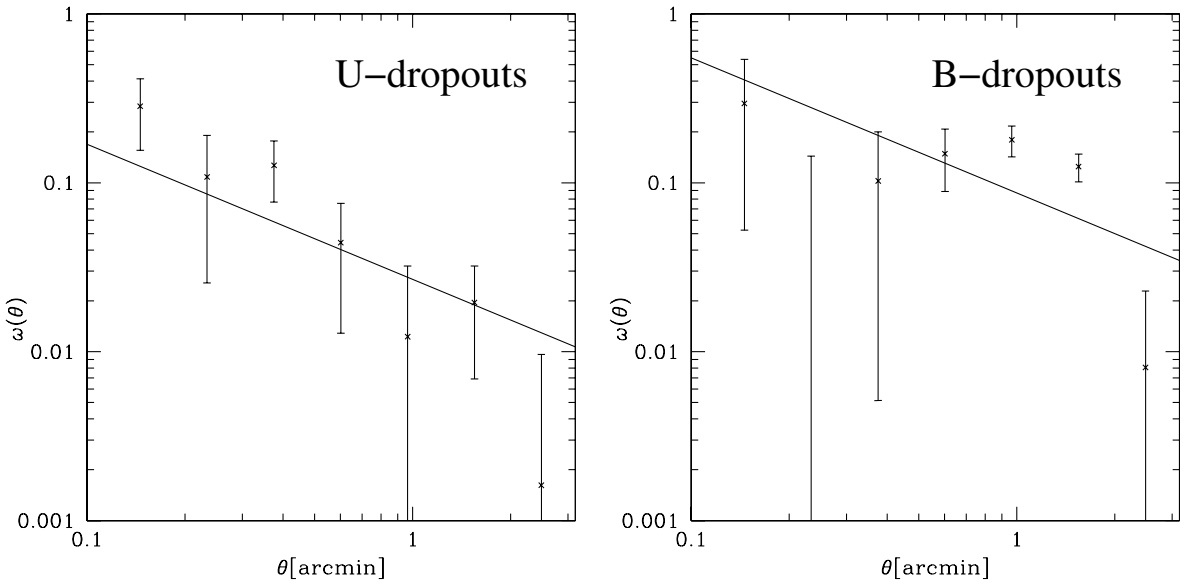

Fig. 11. Angular correlation functions for our U-dropouts (*left*) and our B-dropouts (*right*). The errors are Poissonian errors and the lines represent power-law χ^2 fits to the data with a fixed slope of $\delta = 0.8$. The fitted amplitude at a scale of $1''$ then becomes $A_\omega = 0.71 \pm 0.13$ for the U-dropouts and $A_\omega = 2.31 \pm 0.78$ for the B-dropouts.

magnitude drops to $U \sim 26.4$. Thus some objects which are faint in V could be misclassified as U-dropouts in these regions. For three reasons we believe that this is not the case. First, investigating the distributions of apparent magnitudes in the V- and R-band there is no noticeable difference between the whole sample and the subsample in the shallower regions (288 U-dropouts). If misclassification was present one would see an excess in the faint V-band counts for the subsample. Second, the number density of U-dropouts does not change from deep to shallow regions. Finally, as Steidel et al. (2004) showed, objects that are near in colour space are mostly also near in redshift space so that no spurious clustering signal is expected. A similar consideration applies to the B-dropout sample.

For a known redshift distribution the angular correlation function $\omega(\theta)$ can be related to the real space 3D correlation function $\xi(r)$ using the Limber equation (see Peebles 1980) for a flat universe

$$\omega(\theta) = \int_0^\infty \mathrm{d}\overline{w}\; p^2(\overline{w}) \int_{-\infty}^{\infty} \mathrm{d}\Delta w\; \xi\Big(\sqrt{(\overline{w}\theta)^2 + \Delta w^2}\Big), \qquad (6)$$

Table 2. Clustering measurements. Giavalisco & Dickinson (2001) analysed a photometric sample of U-dropouts extracted from ground-based data. Ouchi et al. (2004b) measured the clustering on their B-dropout sample from the Subaru Deep Survey. The I-band limiting magnitude of our dropout sample is not well known since some objects are not detected in I (see Sect. 3.2).

Sample	Mean redshift	Redshift distribution	Limiting magnitude	r_0 [Mpc h^{-1}]
U-dropouts (this paper)	3.0	flat $2.7 < z < 3.3$	$R_{\mathrm{WFI,Vega}} < 26$	2.0 ± 0.2
U-dropouts (this paper)	3.0	flat $2.6 < z < 3.4$	$R_{\mathrm{WFI,Vega}} < 26$	2.4 ± 0.2
U-dropouts (this paper)	3.0	gauss $\mu = 3.03$, $\sigma = 0.27$	$R_{\mathrm{WFI,Vega}} < 26$	2.6 ± 0.3
Giavalisco & Dickinson (2001)	3.0	from spectroscopic subsample	$\mathcal{R}_{AB} < 25.5 \hat{=} R_{\mathrm{WFI,Vega}} \sim 25.1$	3.2 ± 0.7
B-dropouts (this paper)	3.8	flat $3.7 < z < 4.2$	$I_{\mathrm{WFI,Vega}} \lesssim 26.3$	3.2 ± 0.6
B-dropouts (this paper)	3.8	flat $3.6 < z < 4.3$	$I_{\mathrm{WFI,Vega}} \lesssim 26.3$	3.8 ± 0.7
B-dropouts (this paper)	3.8	gauss $\mu = 3.83$, $\sigma = 0.17$	$I_{\mathrm{WFI,Vega}} \lesssim 26.3$	3.5 ± 0.7
Ouchi et al. (2004b)	4.0	from simulations	$i'_{AB} < 26$	4.1 ± 0.2

where w is the comoving distance, and $\overline{w}$ and Δw are the mean and difference of the comoving distances of the two galaxies considered. $p(\overline{w})$ is the normalised distribution of the galaxies in comoving distance. Usually the real-space correlation function is fitted with a power law with slope $\gamma = \delta + 1$ and correlation length r_0:

$$\xi(r) = \left(\frac{r}{r_0}\right)^{-\gamma}. \quad (7)$$

Thus the second integral can be solved analytically, and the correlation length r_0 then becomes:

$$r_0 = \left[A_{\omega;\mathrm{rad}} \cdot \frac{\Gamma(\gamma/2)}{\Gamma(1/2)\Gamma(\gamma/2 - 1/2)} \cdot \left(\int_0^\infty \mathrm{d}\overline{w}\, p^2(\overline{w})\, \overline{w}^{1-\gamma}\right)^{-1}\right]^{1/\gamma} \quad (8)$$

with $A_{\omega;\mathrm{rad}}$ being the amplitude of the angular correlation function at a scale of one radian (extrapolation), and Γ is the Euler Gamma function.

In order to relate the angular correlation function to the real-space correlation function we need to make an assumption on the redshift distribution. For our dropout samples we choose different redshift distributions to investigate the impact of this uncertain quantity on the correlation lengths. First we assume flat distributions of the source redshifts with different widths. Then we fit a Gaussian to each redshift distribution in Fig. 8 neglecting the secondary peak in the U-dropout redshift distribution. We find that the U-dropout data are well fitted by a Gaussian with mean $z = 3.03$ and a $FWHM = 0.54$ and the B-dropout data by a Gaussian with mean $z = 3.83$ and $FWHM = 0.34$. The errors for the correlation lengths are estimated from the errors of the amplitudes A_ω only, and no effects of the slope or the redshift distributions are taken into account. In Table 2 the results are shown in comparison to other studies by Ouchi et al. (2004b) and Giavalisco & Dickinson (2001). Given the large uncertainties in our redshift distribution and the different depths of the surveys the differences are not significant. Furthermore, within the uncertainties, we do not see an evolution of the scale length from our U-dropout sample to our B-dropout sample. It should be kept in mind that the two populations do not probe the same part of the luminosity function. With a distance modulus of 0.6 mag in a ΛCDM-cosmology between $z = 3$ and $z = 3.8$ and a negligible k-correction between the R-band at $z = 3$ and the I-band at $z = 3.8$[2] the U-dropout sample is slightly deeper in terms of absolute magnitude. It would be desirable to cut the two samples at the same L/L^*-value. But with the available samples being cut at brighter magnitudes (e.g. $R \lesssim 24.6$ for $L \gtrsim L^*$ for the U-dropouts), the statistical errors are still too large to reach significant conclusions. A more sophisticated clustering analysis with dropout samples cut at the same absolute magnitude will be presented when more fields of the DPS are available and LBG numbers have increased.

5. Conclusions and outlook

We find 1070 U- and 565 B-dropout candidates in deep wide-field images of the CDFS taken with the WFI@MPG/ESO2.2m. The photometric redshift distributions are narrowly peaked around $z = 3$ and $z = 4$, as expected. Our number-counts of dropouts in apparent magnitude bins are consistent with previous studies. The angular correlation functions are calculated from the data and correlation lengths are derived taking into account the photometric redshift estimates of the samples. These results are also in good agreement with previous studies showing no evolution from $z \sim 3$ to $z \sim 4$, albeit large systematic errors remain.

The dropout samples in the CDFS will be investigated further. In Sect. 3.2 it was mentioned that ACS@HST images are available for the whole WFI field. The morphology of every candidate will be classified with the help of the high angular resolution of these data; this will yield the largest catalogue of morphologically studied LBGs. Furthermore, infrared data from the GOODS project (Giavalisco et al. 2004) are publicly available. The innermost part of the field (50 arcmin^2) is covered with deep JHK_s images from ISAAC@VLT which will help to improve the photometric redshift accuracy considerably. A larger fraction of the area is covered with shallower data from SOFI@NTT. For the brighter dropouts these data will also be sufficient to improve the photometric redshift estimates.

The aim of this study was to test techniques on the CDFS that will be applied to a much larger dataset, the

[2] Relation between the central wavelengths (CWL): $\mathrm{CWL}_R = 652\,\mathrm{nm} \approx \frac{(1+3)}{(1+3.8)} \cdot \mathrm{CWL}_I = \frac{(1+3)}{(1+3.8)} \cdot 784\,\mathrm{nm}$.

ESO Deep-Public-Survey (DPS). This survey covers three square degrees in total, distributed over three fields of four adjacent WFI pointings each. Deep coverage in the *UBVRI* bands was intended. Unfortunately, the survey was not finished so that now there are only five pointings (1.25 square degrees) complete in all five colours. The completion of five further fields (that are nearly complete) was proposed by us for ESO period 75. First investigations in the four other fields yield a number of U-dropouts each comparable to the CDFS and we proposed a spectroscopic run with VIMOS on one subfield for ESO period 76. There will be several hundreds of LBG spectra to be analysed enabling us to quantify the contamination of our samples, to investigate their redshift distributions, and to study the astrophysical properties in detail. The area of 1.25 square degrees that is completely covered in all five optical bands already now yields a larger LBG sample at $z \sim 3$ than any other study to date. If the DPS is completed, there will be ∼10 000 U-dropouts in the survey on two contiguous fields of one degree width and one of 0.5 degrees width. From these the clustering properties can be studied with unprecedented accuracy on the largest scales up to now and statistics of LBG properties will be improved significantly.

Acknowledgements. This work was supported by the German Ministry for Education and Science (BMBF) through the DLR under the project 50 OR 0106, by the BMBF through DESY under the project 05AE2PDA/8, and by the Deutsche Forschungsgemeinschaft (DFG) under the project SCHN342/3–1.

References

Adelberger, K. L., Steidel, C. C., Shapley, A. E., et al. 2004, ApJ, 607, 226
Arnouts, S., Vandame, B., Benoist, C., et al. 2001, A&A, 379, 740
Bertin, E. 2003, SWarp user's guide
Bertin, E., & Arnouts, S. 1996, A&AS, 117, 393
Bolzonella, M., Miralles, J.-M., & Pelló, R. 2000, A&A, 363, 476
Bruzual, A. G., & Charlot, S. 1993, ApJ, 405, 538
Calzetti, D., Armus, L., Bohlin, R. C., et al. 2000, ApJ, 533, 682
Erben, T., Schirmer, M., Dietrich, J. P., et al. 2005, Astron. Nachr., 326, 432
Foucaud, S., McCracken, H. J., Le Fèvre, O., et al. 2003, A&A, 409, 835
Fruchter, A. S., & Hook, R. N. 2002, PASP, 114, 144
Giavalisco, M. 2002, ARA&A, 40, 579
Giavalisco, M., & Dickinson, M. 2001, ApJ, 550, 177
Giavalisco, M., Ferguson, H. C., Koekemoer, A. M., et al. 2004, ApJ, 600, L93
Kron, R. G. 1980, ApJS, 43, 305
Landy, S. D., & Szalay, A. S. 1993, ApJ, 412, 64
Le Fèvre, O., Vettolani, G., Paltani, S., et al. 2004, 428, 1043
Madau, P. 1995, ApJ, 441, 18
Monet, D. B. A., Canzian, B., Dahn, C., et al. 1998, VizieR Online Data Catalog, 1252, 0
Ouchi, M., Shimasaku, K., Okamura, S., et al. 2004a, ApJ, 611, 660
Ouchi, M., Shimasaku, K., Okamura, S., et al. 2004b, ApJ, 611, 685
Peebles, P. J. E. 1980, The large-scale structure of the universe (Princeton University Press)
Rix, H., Barden, M., Beckwith, S. V. W., et al. 2004, ApJS, 152, 163
Schirmer, M., Erben, T., Schneider, P., et al. 2003, A&A, 407, 869
Steidel, C. C., Adelberger, K. L., Giavalisco, M., Dickinson, M., & Pettini, M. 1999, ApJ, 519, 1
Steidel, C. C., Adelberger, K. L., Shapley, A. E., et al. 2003, ApJ, 592, 728
Steidel, C. C., & Hamilton, D. 1993, AJ, 105, 2017
Steidel, C. C., Shapley, A. E., Pettini, M., et al. 2004, ApJ, 604, 534
Vanzella, E., Cristiani, S., Dickinson, M., et al. 2005, 434, 53
Wolf, C., Meisenheimer, K., Kleinheinrich, M., et al. 2004, A&A, 421, 913